Journal of Materials Chemistry A

ROYAL SOCIETY OF CHEMISTRY

COMMUNICATION

View Article Online
View Journal | View Issue

Cite this: J. Mater. Chem. A, 2024, 12, 19885

Received 29th May 2024
Accepted 24th July 2024

DOI: 10.1039/d4ta03719g

rsc.li/materials-a

Carbon quantum dots-embedded reduced graphene oxide compact films for highly pressure-tolerant electrodes†

Dou Lin,[ab] Ziyan Zhou,[ab] Ronghao Shi,*[c] Bin Chen,[ab] Zhulin Huang,[ab] Haibin Tang,*[ab] Jun Wang,[d] Xiaoguang Zhu,[a] Cheng Shao[a] and Fangming Han*[ab]

High-pressure environments require that power supplies of electronic devices can withstand high pressure without a hard shell. While compact reduced graphene oxide (rGO) electrodes enhance pressure tolerance, they suffer from compromised capacitance and power output due to the decreased ion-accessible surface area and blocked or collapsed ion channels. To overcome this challenge, carbon quantum dots (CQDs) were uniformly embedded into rGO film to create a compact yet porous electrode. This was achieved *via* a hydrothermal reaction to form a rGO/CQDs hydrosol by bonding CQDs to rGO nanosheets, followed by a subsequent vacuum filtering. The "spacer" function of CQDs improves the ion-accessible surface area, ion migration, and compressive strength of the rGO/CQDs films. Molecular dynamics simulations further confirm that embedded CQDs enhance both Young's modulus and the diffusion coefficient of hydronium ions within the rGO/CQDs films. Thus, at an ultra-high pressure of 360 MPa, the prepared rGO/CQDs films retained an impressive 81.2% of their initial capacitance (219.7 F cm^{-3} at 0.8 mA cm^{-2}). The rGO/CQDs-based supercapacitors retained a high volumetric power density of 59.4 W cm^{-3} at 180 MPa. These findings demonstrate the great potential of rGO/CQDs films for pressure-tolerant power supply devices.

Introduction

Pressure-tolerant electronics are vital across diverse fields, from underwater robots to space exploration,[1,2] oil reservoir monitoring,[3,4] and military engineering.[4–6] Electrochemical energy storage (EES) devices play a crucial role in powering pressure-tolerant electronics, influencing their lifespan and effectiveness in high-pressure environments.[1,4] However, the use of rigid pressure vessels to withstand high pressure reduces available space and hinders integration with electronics, especially flexible electronics.[1,7,8] Therefore, there is a need for EES devices that can withstand high pressures without a hard shell. Fortunately, the traditional Chinese philosophy of Taichi, advocating the "softness overcoming hardness", offers a "soft" solution to the "hard" problem.

Supercapacitors made of graphene nanosheets have emerged as promising EES devices due to their high power density, fast charging and long lifespan.[9–13] However, the low packing density (<0.8 g cm^{-3}) of carbon electrodes commonly used in supercapacitors[14–16] makes them susceptible to damage under compressive pressure. Though compact electrodes with high volumetric capacitance prepared by a capillary shrinkage method can withstand tens-MPa pressure,[17–19] this issue has still not been completely solved. This is because high pressure can lead to degraded capacitance and power density of dense electrodes due to reduced ion-accessible surface area and block or collapse of ion transport pathways.

One effective method to prevent graphene nanosheets from irreversibly π–π stacking is by introducing "spacers" within the film.[20,21] These spacers maintain smooth ion migration channels, crucial for high power applications. Various carbon-based nanomaterials like carbon nanoparticles,[22] nanotubes,[23] nanofibers[21] and nanosheets[24] have been used as spacers through mechanical mixing and vacuum filtration. This embedding creates graphene composites with a larger ion-accessible surface, enhancing both capacitance and power capability. However, this approach comes with a trade-off. Physically mixing spacers with graphene nanosheets weakens the crucial interlayer interaction between graphene nanosheets and thus reduces the overall mechanical strength of the film.[25–27] The weakening effect is more pronounced with larger spacers. Therefore, selecting smaller-sized spacers is critical to both strengthen the interlayer

[a]Key Laboratory of Materials Physics, Anhui Key Laboratory of Nanomaterials and Nanostructures, Institute of Solid State Physics, HFIPS, Chinese Academy of Sciences, Hefei, 230031, P. R. China. E-mail: fmhan@issp.ac.cn; hbtang@issp.ac.cn
[b]University of Science and Technology of China, Hefei, 230026, P. R. China
[c]Henan Key Laboratory of Advanced Conductor Materials, Institute of Materials, Henan Academy of Sciences, Zhengzhou 450046, P. R. China. E-mail: smartsrh@hnas.ac.cn
[d]State Key Laboratory of Nonlinear Mechanics, Institute of Mechanics, Chinese Academy of Sciences, Beijing 100190, P. R. China

† Electronic supplementary information (ESI) available. See DOI: https://doi.org/10.1039/d4ta03719g

interactions and improve the compressive strength of the composite films. Additionally, smaller nanometer-sized spacers can achieve high packing density[23,28] while providing more mesopore spaces. This combination further improves volumetric capacitance and power performance. Carbon quantum dots (CQDs), with their nanometer-sized diameter, offer a promising solution. These CQDs exhibit typical electric double layer behavior,[29] excellent water-solubility,[30] chemical stability,[31,32] and readily functional surface groups.[29,33] Previous works have demonstrated that through a series of complex preparation processes, CQDs could be successfully bonded to reduced graphene oxide (rGO) sheets, forming rGO/CQDs powders.[31] While electrodes fabricated by mixing rGO/CQDs powders with carbon black and polyvinylidene fluoride binder typically exhibit a higher gravimetric capacitance than rGO alone,[31] these non-integral electrodes cannot withstand high pressure due to the potential mechanical degradation of the carbon black and binder.[34] Despite some progress, the impact of CQDs on the pressure tolerance of rGO-based electrodes remains largely unexplored.

This study presents a novel synthesis creates a colloidal solution of rGO/CQDs hybrid nanosheets made from GO and CQDs,[31,35] which is then vacuum-filtered into integral rGO/CQDs films, avoiding any conductive agent or binder. The embedded CQDs create mesopores in the rGO/CQDs films, boosting their volumetric capacitance. Additionally, the spacing action of the CQDs significantly enhances the films' electrochemical performance and compressive strength, which is confirmed by the improved diffusion coefficient of hydronium ions (3.0×10^{-9} m^2 s^{-1}) and Young's modulus (5.1 GPa) obtained from the molecular dynamics simulations. Consequently, the rGO/CQDs-based supercapacitors exhibit remarkable electrochemical stability and high power density even under high pressure, demonstrating their potentials for pressure-tolerant power supply devices.

Results and discussion

Fabrication and characterizations of the rGO/CQDs composites

Fig. 1a depicts the synthesis of the rGO/CQDs films. As reported in literatures, both GO and CQDs possess carboxyl and phenolic hydroxyl groups on their surfaces.[36–39] These functional groups on the surfaces leave negative charges,[36] enabling them to form stable colloids due to their electrostatic repulsion (Fig. 1b). An aqueous solution containing a dilute mixture of GO and CQDs (a total concentration of 0.05 mg ml^{-1}) was heated in a sealed autoclave at 185–200 °C for 3 hours. This hydrothermal process facilitates chemical reaction between GO and CQDs, leading to the uniform attachment of CQDs onto the rGO surface.[31,35] Notably, the rGO/CQDs nanosheets are still negatively charged, as shown in Fig. 1c, and the inset further corroborates their colloidal nature by depicting the Tyndall effect observed in the rGO/CQDs dispersion. Fourier transform infrared (FTIR) spectra (Fig. 1d) shows a decrease in the peak intensities of the C–O (hydroxyl) groups at ~1050 cm^{-1} and the C=O (carboxyl) groups at ~1720 cm^{-1} for the rGO/CQDs. This suggests a reduction of these functional groups. However, still other groups remain, as evidenced by the peaks at ~1390 cm^{-1} (O–H of carboxyl) and ~3370 cm^{-1} (–OH vibrations of surface-adsorbed water).[38,40] Since oxygen functional groups primarily reside on the surface of the CQDs and GO, their reactions primarily occur as follows:[41,42]

$$GO - COOH + CQDs - OH \rightarrow rGO - CQDs + CO_2 + H_2O, \quad (1)$$

$$GO - OH + CQDs - COOH \rightarrow rGO - CQDs + CO_2 + H_2O. \quad (2)$$

This aligns with the observed decreases in C=O (carboxyl) and –OH functional group signals in the FTIR spectra (Fig. 1d). Similar phenomena have been documented previously for carbon nanotubes, CQDs and graphene sheets.[41–44] The high hydrothermal temperature (185–200 °C) likely facilitates this decarboxylation/condensation reaction, leading to a significant reduction in the –OH peak intensity in the FTIR spectra. Finally, the rGO/CQDs films were obtained by vacuum filtration of the rGO/CQDs colloids (Fig. 1a and S1†).

Transmission electron microscope (TEM) images reveal the uniform attachment of 3–6 nm sized CQDs onto the rGO surfaces (Fig. 2a and S2†) after the hydrothermal treatment. Scanning electron microscopy (SEM) images (inset in Fig. 2a and S3†) further demonstrate a uniform film thickness with a compact, layered stacking morphology and a smooth surface. Notably, the presence of CQDs effectively prevents restacking of rGO nanosheets. Consequently, the rGO/CQDs hybrid film boasts a significantly higher specific surface area (142 m^2 g^{-1}) and pore volume (0.28 cm^3 g^{-1}) compared with the rGO film (82 m^2 g^{-1} and 0.15 cm^3 g^{-1}) (Fig. 2b and c). X-ray photoelectron spectroscopy (XPS) analysis (Fig. S4†) confirms the presence of carbon (C) and oxygen (O) elements in GO, CQDs and rGO/CQDs. High-resolution C 1s spectra (Fig. 2d–f) of all three materials show prominent peaks at 284.6, 286.2 and 288.8 eV, corresponding to C=C/C–C, C–O, and C=O bonds, respectively.[13,45,46] Remarkably, the rGO/CQDs possess a higher C=C/C–C content in contrast to that of GO and CQDs. Conversely, the C–O and C=O contents in rGO/CQDs are lower than those observed in GO and CQDs. This observation aligns well with the findings from FTIR analysis (Fig. 1d), suggesting a successful

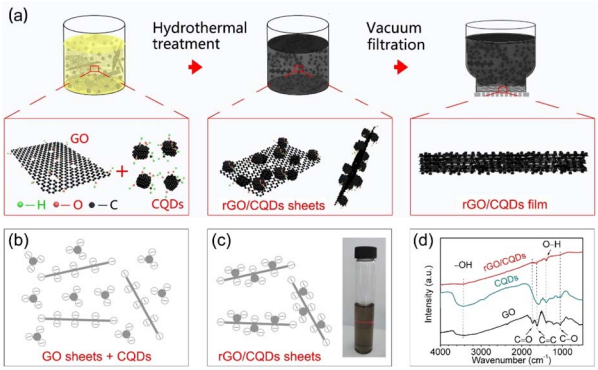

Fig. 1 (a) Schematic fabrication process of the rGO/CQDs films. (b) Mixed colloids of CQDs and GO nanosheets. (c) Stable colloids of rGO/CQDs nanosheets. (d) FTIR spectra of GO, CQDs and the rGO/CQDs nanosheets.

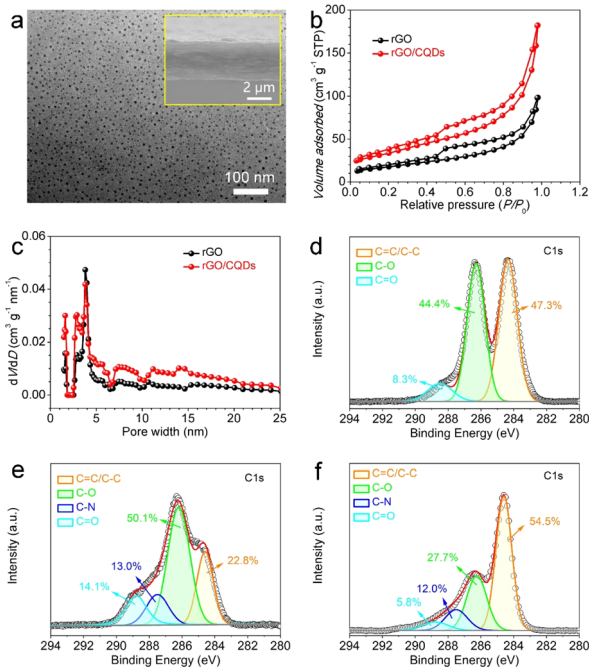

Fig. 2 Materials characterization. (a) TEM image of the rGO/CQDs nanosheets (the inset is a cross-sectional SEM image of the rGO/CQDs). (b) N_2 adsorption–desorption isotherms (STP). (c) Pore-size distribution. (d–f) C 1s XPS spectra of the GO (d), CQDs (e) and rGO/CQDs (f). The crude material mass ratio of CQDs/GO is 0.4 for the rGO/CQDs.

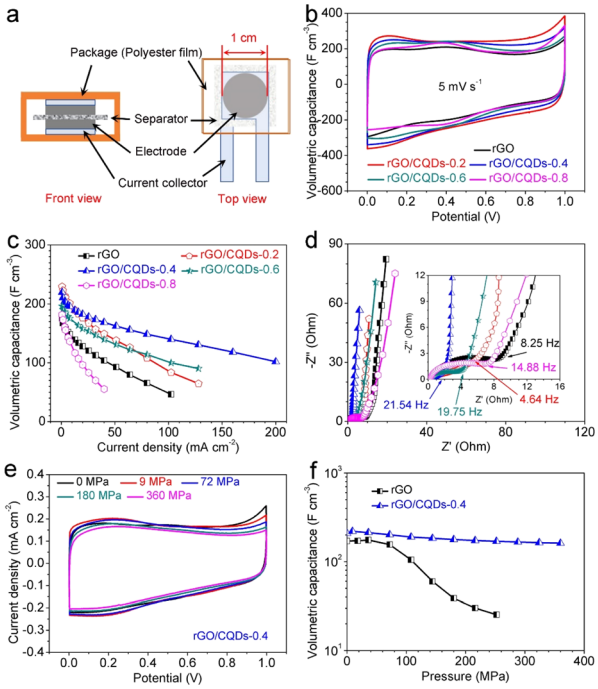

Fig. 3 Electrochemical performances of the rGO/CQDs films with increasing pressure. (a) Schematic of a sandwich-configuration supercapacitor. (b) CV curves at 5 mV s^{-1} without pressure. (c) Volumetric capacitances at different current densities. (d) Nyquist plots without pressure. (e) CV curves at 5 mV s^{-1} varying with pressure. (f) Volumetric capacitances of the rGO and rGO/CQDs-0.4 at 0.8 mA cm^{-2} *versus* pressure.

decarboxylation/condensation reaction between –COOH and –OH groups on the surface of the CQDs and GO during hydrothermal treatment. Additionally, both CQDs and rGO/CQDs exhibit trace amounts of C–N bond (peaks at 287.5 eV). The presence of trace N-element likely originates from the peanut shells used as precursors for the CQDs.[47]

Electrochemical performances of the rGO/CQDs films with increasing pressure

Pressure tolerance is vital for electrode materials in energy storage device, particularly those served in autonomous underwater vehicles,[1,2] as it directly affects their operational lifespan. This study investigates the pressure tolerance of rGO/CQDs compact films with varying CQDs contents (labeled as "rGO/CQDs-*X*", where *X* represents the mass ratio of CQDs to GO in the crude materials). To assess electrode stability under high pressure, these films were assembled into sandwich-configuration supercapacitors (Fig. 3a and S5†). These supercapacitors were subjected to static pressures ranging from 0 to 360 MPa (Fig. S6, and Table S1†). To evaluate the effect of the separator on electrochemical properties under pressures, pure Pt foil-based supercapacitor was tested across the same pressure range. The results demonstrated minimal influence of the separator on the electrochemical performance under pressure, as the Pt foil exhibits only a slight decrease in capacitance with increasing pressure (Fig. S7 and S8†).

Under zero applied pressure, the rGO/CQDs films display approximate-rectangular cyclic voltammetry (CV) curves at a scan rate of 5 mV s^{-1} (Fig. 3b), indicating excellent electrical double-layer capacitive behavior. This characteristic is further confirmed by the near-isosceles triangular galvanostatic charge–discharge (GCD) curves at a current density of 0.8 mA cm^{-2} (Fig. S9a and S10†). Even at a high current density of 40 mA cm^{-2}, the GCD curve of rGO/CQDs-0.4 demonstrates superior rate capability with the smallest *IR* drop among all electrodes (Fig. 3c and S9b†). Its volumetric capacitance reaches 219.7 F cm^{-3} at 0.8 mA cm^{-2}, which is slightly lower than that of rGO/CQDs-0.2 but higher than that of rGO. This superior performance could be attributed to the larger ion-accessible surface area and wider ion channels created by the incorporation of CQDs within the rGO/CQDs films (Fig. S11†). Furthermore, the Nyquist plot (Fig. 3d) reveals a smaller-diameter semicircle for the rGO/CQDs-0.4 electrode compared with that of the rGO and other rGO/CQDs electrodes, signifying its improved efficiency for ion migration.[14,48] Consequently, the rGO/CQDs-0.4-based supercapacitors achieve outstanding volumetric power densities of 249.1 W cm^{-3} and 170.1 W cm^{-3} in 1 M H_2SO_4 and 6 M KOH aqueous electrolytes, respectively, significantly higher than rGO- and other carbon-based supercapacitors (Fig. S12 and Tabel S2†).[19,20,41,49–59]

Further, as pressure increases (Fig. 3e), the CV curve of rGO/CQDs-0.4 shows minimal shape change, indicating excellent electrochemical stability under varying pressures. In contrast, the CV curves of rGO and other rGO/CQDs electrodes experience

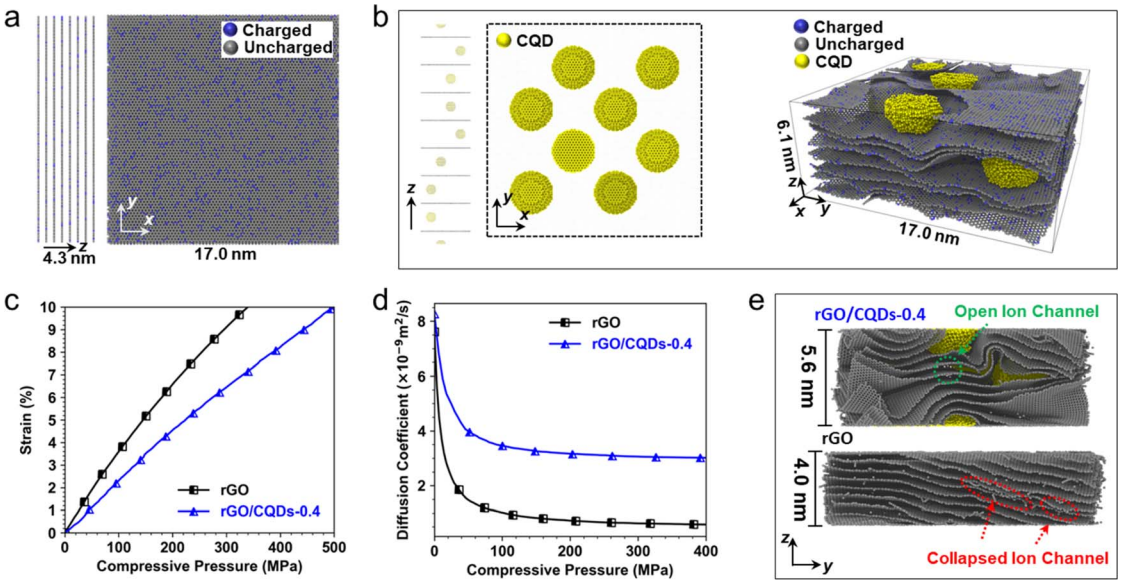

Fig. 4 Molecular dynamics simulations of rGO and rGO/CQDs-0.4 films in aqueous electrolyte under pressure. (a) Initial configuration of the simulated rGO film. Blue and gray atoms present charged and uncharged carbon atoms, respectively. (b) Positions of interlayer CQDs and inherent structure of the simulated rGO/CQDs-0.4 film generated using the conjugate-gradient method. (c) Compressive strain of rGO and rGO/CQDs-0.4 *versus* compressive pressure. (d) Diffusion coefficients of hydronium ions within rGO and rGO/CQDs-0.4 *versus* compressive pressure. (e) Snapshot of the simulated rGO and rGO/CQDs-0.4 films filled with aqueous electrolyte at a compressive strain of 8.0% (360 MPa). Only carbon atoms are kept to visualize the deformed structures of film.

significant shape change at elevated pressure (Fig. S13†). Specifically, rGO/CQDs-0.4 retains a remarkable 81.2% of its capacitance even at 360 MPa (161.3 F cm^{-3}), significantly surpassing that of rGO film (14.8%, 25.4 F cm^{-3} at 252 MPa) and other rGO/CQDs with varying CQDs contents (Fig. 3f and S14†). This exceptional performance stands out among all compression-resistant electrodes.[60–64] Furthermore, rGO/CQDs-0.4 displays superior rate capability and power performance (59.4 W cm^{-3}) at 180 MPa compared to rGO and other rGO/CQDs samples (Fig. S15†). The rGO/CQDs-0.4 also yields a lower resistance to charge transfer (R_{ct}) at 9 MPa than that at 0 MPa (Fig. S16†), indicating a faster rate of ion transport under pressure.[14,65] Even with increasing pressure from 9 to 360 MPa, the R_{ct} of rGO/CQDs-0.4 only lifts slightly (from 0.5 to 2.9 ohm), demonstrating its superior pressure tolerance (Fig. S16†) than that of rGO (Fig. S17†) again. Meanwhile, rGO/CQDs-0.4 electrodes fabricated with CQDs synthesized with different precursors also demonstrate superior pressure tolerances, highlighting the universality of various CQD precursor materials (Fig. S18–S20†). Moreover, the rGO/CQDs-0.4-based supercapacitor retains 95.4 and 98.2% of its capacitance after 50 000 cycles under 36 and 180 MPa, respectively (Fig. S21†). Even after pressure is removed for 12 hours, it still exhibits almost 100% capacitance recovery (Fig. S22†), indicating its suitability for high-pressure applications. These findings make the rGO/CQDs-0.4-based supercapacitor promising for energy storage in harsh environments. Potential applications include power supply devices for autonomous underwater vehicles,[1,2] module for wireless sensors monitoring hydraulic fracture and oil reservoirs,[3,4] and modules for hybrid military vehicles in specialized applications.[5,6]

Molecular dynamics simulations

To understand the mechanism behind the higher pressure tolerance of rGO/CQDs-0.4 film than that of rGO film, large-scale molecular massively parallel simulation[66] was employed. The simulations focused on a 1 M H_2SO_4 aqueous electrolyte (considering only hydronium ion transport due to the Grotthuss mechanism[67]) and the carbon electrode atoms. The results were visualized using OVITO software.[68]

This mode is based on two primary assumptions, namely first that the rGO sheet within the film is flat and evenly separated, and second, that both rGO and CQDs consist solely of carbon (detailed illustration in Fig. S23†). Under high pressure, the electrodes are expected to deform, potentially inducing mobility in the carbon atoms. To accommodate this, the carbon atoms in the molecular dynamics model are not fixed during the simulation. The rGO film was simplified as 8 negatively charged graphene sheets, each composed of 11 200 carbon atoms (~17 × 17 nm^2 in x–y plain) and carrying a charge density of −0.42C m^{-2}. This configuration maintains an average interlayer spacing of 0.54 nm in the absence of applied pressure (Fig. 4a and S23†).[12] For the rGO/CQDs-0.4 film, the model, adjusted using the conjugate-gradient method post-compression and relaxation, includes 8 similarly charged graphene sheets embedded with 8 CQDs (each between two neighboring graphene sheets has 2773 carbon atoms and a spherical graphite structure with a radius of ~2 nm) as spacers, resulting in an average interlayer spacing of 0.76 nm (Fig. 4b).

The simulations effectively capture how the strain within the rGO and rGO/CQDs-0.4 films (Fig. 4c) and the diffusion coefficients of hydronium ions inside them (Fig. 4d) change with pressure (detailed process in Fig. S24†). Notably, the simulations

unveil a higher Young's modulus for the rGO/CQDs-0.4 film (5.1 GPa) other than the rGO film (3.4 GPa, Fig. 4c), confirming its superior pressure tolerance. Furthermore, the rGO/CQDs-0.4 film always exhibits a higher diffusion coefficient of hydronium ions with increasing compressive pressure compared with the rGO film. Even at a high pressure of 360 MPa, the rGO/CQDs-0.4 film maintains a significantly higher diffusion coefficient (3.0×10^{-9} m^2 s^{-1}) than the rGO film does (0.6×10^{-9} m^2 s^{-1}). This difference can be attributed to the collapse of ion channels within the rGO film under ultrahigh pressure, while the rGO/CQDs-0.4 film retains open channels (Fig. 4e). Therefore, the simulations convincingly demonstrate the superior pressure tolerance of rGO/CQDs-0.4 to that of rGO, aligning perfectly with the experimental findings.

Conclusions

In summary, we have successfully developed rGO/CQDs hybrid compact films with exceptional compressive strength by combining hydrothermal method with vacuum filtration. The strong connection between rGO nanosheets and CQDs prevents the nano-porous structure from collapsing under high pressure. The insertion of CQDs into the rGO matrix further enhances the ion-accessible specific surface area within the electrode, resulting in a high volumetric capacitance of 219.7 F cm^{-3} at 0.8 mA cm^{-2}. Moreover, acting as spacers, the CQDs significantly improve ion migration and heighten the compressive strength of the rGO/CQDs hybrid films, as evidenced by the significantly improved diffusion coefficient of hydronium ions and Young's modulus obtained from the molecular dynamics simulations, ensuring good electrochemical stability and high power capability under high pressure. Consequently, these rGO/CQDs-based supercapacitors provide great potential for compact energy storage devices and pressure-tolerant electronics, offering valuable insights into the development of high-performance supercapacitors.

Data availability

All data supporting the findings of this study are available within the paper and its ESI.†

Author contributions

Dou Lin: investigation, methodology, writing. Ziyan Zhou: data curation, methodology. Ronghao Shi: supervision, software, writing – review & editing. Bin Chen: data curation, methodology. Zhulin Huang: software, data curation. Haibin Tang: data curation, supervision, writing – review & editing. Jun Wang: visualization, software. Xiaoguang Zhu: visualization, validation. Cheng Shao: visualization, validation. Fangming Han: investigation, methodology, writing, supervision, project administration, funding acquisition, writing – review & editing. All authors discussed the results and approved the final version of the paper.

Conflicts of interest

There are no conflicts to declare.

Acknowledgements

This work was supported by Natural Science Foundation of China (Grant No. 52072372, 52372241, 52222208), the Hefei Institute of Physical Science Director's Fund (Grant No. BJPY2023A07, YZJJ-GGZX-2022-01, BJPY2022B03), the Scientific and Technological Research Project of Henan Academy of Sciences (Project No. 242217018), and the Startup Research Fund of Henan Academy of Sciences (Project No. 231817007).

References

1 M. Li, Y. Hu, C. Lu, B. Li, W. Tian, J. Zhang and Z. Mao, *J. Energy Storage*, 2022, **54**, 105325.
2 A. Sahoo, S. K. Dwivedy and P. S. Robi, *Ocean Eng.*, 2019, **181**, 145–160.
3 C. H. Martins, A. A. Alshehri and I. F. Akyildiz, *IEEE 8th Annual UEMCON*, 2017, pp. 434–441.
4 B. O. Vishwanath, N. Vedachalam, P. Muthuvel, K. Jayanthi and G. A. Ramadass, *Mar. Technol. Soc. J.*, 2018, **52**, 110–117(118).
5 A. A. Mamun, Z. Liu, D. M. Rizzo and S. Onori, *IEEE Trans. Transp. Electrif.*, 2019, **5**, 239–251.
6 Y. Zhou, H. Qi, J. Yang, Z. Bo, F. Huang, M. S. Islam, X. Lu, L. Dai, R. Amal, C. H. Wang and Z. Han, *Energy Environ. Sci.*, 2021, **14**, 1854–1896.
7 C.-w. Zheng, S.-y. Zhou, Z.-q. Chen, Y.-l. Ge, D.-y. Huang, J. Liu and Q. Yang, *J. Zhejiang Univ., Sci., A*, 2018, **19**, 774–785.
8 Y. Yang, K.-P. Wang, Q. Zang, Q. Shi, Y. Wang, Z. Xiao, Q. Zhang and L. Wang, *J. Mater. Chem. A*, 2022, **10**, 11277–11287.
9 W. Chen, J. Gu, Q. Liu, M. Yang, C. Zhan, X. Zang, T. A. Pham, G. Liu, W. Zhang, D. Zhang, B. Dunn and Y. Morris Wang, *Nat. Nanotechnol.*, 2022, **17**, 153–158.
10 Y. Xia, T. S. Mathis, M.-Q. Zhao, B. Anasori, A. Dang, Z. Zhou, H. Cho, Y. Gogotsi and S. Yang, *Nature*, 2018, **557**, 409–412.
11 Y. Zhu, S. Murali, M. D. Stoller, K. J. Ganesh, W. Cai, P. J. Ferreira, A. Pirkle, R. M. Wallace, K. A. Cychosz, M. Thommes, D. Su, E. A. Stach and R. S. Ruoff, *Science*, 2011, **332**, 1537.
12 X. Yang, C. Cheng, Y. Wang, L. Qiu and D. Li, *Science*, 2013, **341**, 534.
13 D. Lin, Z. Tang, Q. Pan, S. Zhang, D. Huo, S. Yan and F. Han, *ChemElectroChem*, 2020, **7**, 1987–1991.
14 Y. Shao, M. F. El-Kady, C. W. Lin, G. Zhu, K. L. Marsh, J. Y. Hwang, Q. Zhang, Y. Li, H. Wang and R. B. Kaner, *Adv. Mater.*, 2016, **28**, 6719–6726.
15 S. Yuan, W. Fan, D. Wang, L. Zhang, Y.-E. Miao, F. Lai and T. Liu, *J. Mater. Chem. A*, 2021, **9**, 423–432.
16 F. Chi, C. Li, Q. Zhou, M. Zhang, J. Chen, X. Yu and G. Shi, *Adv. Energy Mater.*, 2017, **7**, 1700591.
17 H. Li, Y. Tao, X. Zheng, J. Luo, F. Kang, H.-M. Cheng and Q.-H. Yang, *Energy Environ. Sci.*, 2016, **9**, 3135–3142.
18 Y. Xu, Y. Tao, H. Li, C. Zhang, D. Liu, C. Qi, J. Luo, F. Kang and Q.-H. Yang, *Nano Energy*, 2017, **36**, 349–355.
19 P. Li, H. Li, D. Han, T. Shang, Y. Deng, Y. Tao, W. Lv and Q.-H. Yang, *Adv. Sci.*, 2019, **6**, 1802355.

20 M. Beidaghi and C. Wang, *Adv. Funct. Mater.*, 2012, **22**, 4501–4510.
21 H. Luo, P. Xiong, J. Xie, Z. Yang, Y. Huang, J. Hu, Y. Wan and Y. Xu, *Adv. Funct. Mater.*, 2018, **28**, 1803075.
22 X.-Y. Fu, D.-L. Chen, Y. Liu, H.-B. Jiang, H. Xia, H. Ding and Y.-L. Zhang, *ACS Appl. Nano Mater.*, 2018, **1**, 777–784.
23 D. T. Pham, T. H. Lee, D. H. Luong, F. Yao, A. Ghosh, V. T. Le, T. H. Kim, B. Li, J. Chang and Y. H. Lee, *ACS Nano*, 2015, **9**, 2018–2027.
24 Z.-S. Wu, S. Yang, L. Zhang, J. B. Wagner, X. Feng and K. Müllen, *Energy Storage Mater.*, 2015, **1**, 119–126.
25 E. Gao, Y. Cao, Y. Liu and Z. Xu, *ACS Appl. Mater. Interfaces*, 2017, **9**, 24830–24839.
26 H. Qin, W. Tong, Q.-X. Pei, Z. Wang, G. Zhang, Y. Chen, P. Li, J. Liu, Z. Xu and Y. Liu, *Adv. Funct. Mater.*, 2023, **33**, 2300210.
27 E. Jin, J. He, K. Sheng, Z. Zhang, G. Shi and Q. Zheng, *Acta Mater.*, 2013, **61**, 6466–6473.
28 Y. Yuan, L. Jiang, X. Li, P. Zuo, X. Zhang, Y. Lian, Y. Ma, M. Liang, Y. Zhao and L. Qu, *Adv. Mater.*, 2022, **34**, 2110013.
29 Z. Pan, H. Zhi, Y. Qiu, J. Yang, L. Xing, Q. Zhang, X. Ding, X. Wang, G. Xu, H. Yuan, M. Chen, W. Li, Y. Yao, N. Motta, M. Liu and Y. Zhang, *Nano Energy*, 2018, **46**, 266–276.
30 H. Li, X. He, Z. Kang, H. Huang, Y. Liu, J. Liu, S. Lian, C. H. A. Tsang, X. Yang and S.-T. Lee, *Angew. Chem., Int. Ed.*, 2010, **49**, 4430–4434.
31 Y.-Q. Dang, S.-Z. Ren, G. Liu, J. Cai, Y. Zhang and J. Qiu, *Nanomaterials*, 2016, **6**, 212.
32 S. Zhang, L. Sui, H. Dong, W. He, L. Dong and L. Yu, *ACS Appl. Mater. Interfaces*, 2018, **10**, 12983–12991.
33 M. L. Wang and F. M. Han, *J. Alloys Compd.*, 2017, **727**, 991–997.
34 K. Takahashi, K. Higa, S. Mair, M. Chintapalli, N. Balsara and V. Srinivasan, *J. Electrochem. Soc.*, 2016, **163**, A385.
35 W. Wan, L. Li, Z. Zhao, H. Hu, X. Hao, D. A. Winkler, L. Xi, T. C. Hughes and J. Qiu, *Adv. Funct. Mater.*, 2014, **24**, 4915–4921.
36 D. Li, M. B. Muller, S. Gilje, R. B. Kaner and G. G. Wallace, *Nat. Nanotechnol.*, 2008, **3**, 101–105.
37 Y. C. Yen, C. C. Lin, P. Y. Chen, W. Y. Ko, T. R. Tien and K. J. Lin, *R. Soc. Open Sci.*, 2017, **4**, 161051.
38 T. Szabo, O. Berkesi, P. Forgo, K. Josepovits, Y. Sanakis, D. Petridis and I. Dekany, *Chem. Mater.*, 2006, **18**, 2740–2749.
39 A. C. Lokhande, I. A. Qattan, C. D. Lokhande and S. P. Patole, *J. Mater. Chem. A*, 2020, **8**, 918–977.
40 H.-L. Guo, X.-F. Wang, Q.-Y. Qian, F.-B. Wang and X.-H. Xia, *ACS Nano*, 2009, **3**, 2653–2659.
41 S. Zhang, J. Zhu, Y. Qing, L. Wang, J. Zhao, J. Li, W. Tian, D. Jia and Z. Fan, *Adv. Funct. Mater.*, 2018, **28**, 1805898.
42 M. A. Kabbani, V. Kochat, S. Bhowmick, M. Soto, A. Som, K. R. Krishnadas, C. F. Woellner, Y. M. Jaques, E. V. Barrera, S. Asif, R. Vajtai, T. Pradeep, D. S. Galvão, A. T. Kabbani, C. S. Tiwary and P. M. Ajayan, *Carbon*, 2018, **134**, 491–499.
43 M. A. Kabbani, C. S. Tiwary, A. Som, K. R. Krishnadas, P. A. S. Autreto, S. Ozden, K. Keyshar, K. Hackenberg, A. C. Chipara, D. S. Galvao, R. Vajtai, A. T. Kabbani, T. Pradeep and P. M. Ajayan, *Carbon*, 2016, **104**, 196–202.
44 M. A. Kabbani, C. S. Tiwary, P. A. S. Autreto, G. Brunetto, A. Som, K. R. Krishnadas, S. Ozden, K. P. Hackenberg, Y. Gong, D. S. Galvao, R. Vajtai, A. T. Kabbani, T. Pradeep and P. M. Ajayan, *Nat. Commun.*, 2015, **6**, 7291.
45 L. Li, Y. Li, Y. Ye, R. Guo, A. Wang, G. Zou, H. Hou and X. Ji, *ACS Nano*, 2021, **15**, 6872–6885.
46 X. Xu, J. Yang, X. Zhou, S. Jiang, W. Chen and Z. Liu, *Chem. Eng. J.*, 2020, **397**, 125525.
47 M. Xue, Z. Zhan, M. Zou, L. Zhang and S. Zhao, *New J. Chem.*, 2016, **40**, 1698–1703.
48 I. Shitanda, S. Tsujimura, H. Yanai, Y. Hoshi and M. Itagaki, *Electrochemistry*, 2015, **83**, 335–338.
49 Y. Tao, X. Xie, W. Lv, D.-M. Tang, D. Kong, Z. Huang, H. Nishihara, T. Ishii, B. Li, D. Golberg, F. Kang, T. Kyotani and Q.-H. Yang, *Sci. Rep.*, 2013, **3**, 2975.
50 J. Zhong, W. Sun, Q. Wei, X. Qian, H.-M. Cheng and W. Ren, *Nat. Commun.*, 2018, **9**, 3484.
51 J. Ouyang, X. Wang, L. Wang, W. Xiong, M. Li, Z. Hua, L. Zhao, C. Zhou, X. Liu, H. Chen and Y. Luo, *Carbon*, 2022, **196**, 532–539.
52 L. Sheng, J. Chang, L. Jiang, Z. Jiang, Z. Liu, T. Wei and Z. Fan, *Adv. Funct. Mater.*, 2018, **28**, 1800597.
53 Y. Yoon, K. Lee, S. Kwon, S. Seo, H. Yoo, S. Kim, Y. Shin, Y. Park, D. Kim, J.-Y. Choi and H. Lee, *ACS Nano*, 2014, **8**, 4580–4590.
54 H. Li, D. Yuan, C. Tang, S. Wang, J. Sun, Z. Li, T. Tang, F. Wang, H. Gong and C. He, *Carbon*, 2016, **100**, 151–157.
55 M. F. El-Kady and R. B. Kaner, *Nat. Commun.*, 2013, **4**, 1475.
56 J. Lin, Z. Peng, Y. Liu, F. Ruiz-Zepeda, R. Ye, E. L. G. Samuel, M. J. Yacaman, B. I. Yakobson and J. M. Tour, *Nat. Commun.*, 2014, **5**, 5714.
57 V. Strauss, K. Marsh, M. D. Kowal, M. El-Kady and R. B. Kaner, *Adv. Mater.*, 2018, **30**, 1704449.
58 T. Gao, Z. Zhou, J. Yu, J. Zhao, G. Wang, D. Cao, B. Ding and Y. Li, *Adv. Energy Mater.*, 2019, **9**, 1802578.
59 H. Chen, T. Liu, J. Mou, W. Zhang, Z. Jiang, J. Liu, J. Huang and M. Liu, *Nano Energy*, 2019, **63**, 103836.
60 H. Li, Y. Tao, X. Zheng, Z. Li, D. Liu, Z. Xu, C. Luo, J. Luo, F. Kang and Q.-H. Yang, *Nanoscale*, 2015, **7**, 18459–18463.
61 Z. Niu, W. Zhou, X. Chen, J. Chen and S. Xie, *Adv. Mater.*, 2015, **27**, 6002–6008.
62 W. Sun, Y. Zhang and F. Yang, *Electrochim. Acta*, 2020, **357**, 136874.
63 M. Han, X. Wang, C. Chen, M. Zou, Z. Niu, Q.-H. Yang, A. Cao, L. Song, J. Chen and S. Xie, *Energy Storage Mater.*, 2018, **13**, 119–126.
64 X. Liang, K. Nie, X. Ding, L. Dang, J. Sun, F. Shi, H. Xu, R. Jiang, X. He, Z. Liu and Z. Lei, *ACS Appl. Mater. Interfaces*, 2018, **10**, 10087–10095.
65 X. Li, J. Rong and B. Wei, *ACS Nano*, 2010, **4**, 6039–6049.
66 S. Plimpton, *J. Comput. Phys.*, 1995, **117**, 1–19.
67 C. Knight and G. A. Voth, *Acc. Chem. Res.*, 2012, **45**, 101–109.
68 A. Stukowski and K. Albe, *Modell. Simul. Mater. Sci. Eng.*, 2010, **18**, 085001.

